OXFORD

Journal of Geophysics and Engineering

Journal of Geophysics and Engineering (2019) **16**, 1071–1083 doi:10.1093/jge/gxz067

Non-orthogonal beam coordinate system wave propagation and reverse time migration

Zhaolin Zhu[1,2], **Danping Cao**[1,2,*], **Bangyu Wu**[3], **Xingyao Yin**[1,2] **and Ying Wang**[4]

[1] School of Geosciences, China University of Petroleum (East China), 66 Changjiang Xi Road, Huangdao District, Qingdao City, Shandong Province 266580, China
[2] Laboratory for Marine Mineral Resources, Qingdao National Laboratory for Marine Science and Technology, 1# Wenhai Road, Jimo District, Qingdao 266071, China
[3] School of Mathematics and Statistics, Xi'an Jiaotong University, 28 Xianning West Road, Beilin District, Xi'an City, Shaanxi Province 710049, China
[4] Department of Geoscience and Petroleum, Norwegian University of Science and Technology, NTNU, S.P. Andersens vei 15A, 7491, Trondheim, Norway

[*] Corresponding author: Danping Cao. E-mail: caodp@upc.edu.cn

Received 30 May 2019, revised 11 July 2019
Accepted for publication 8 August 2019

Abstract

Grid size has a significant influence on the computation efficiency and accuracy of finite-difference seismic modeling and can change the workload of reverse time migration (RTM) remarkably. This paper proposes a non-orthogonal analytical coordinate system, beam coordinate system (BCS), for the solution of seismic wave propagation and RTM. Starting with an optical Gaussian beam width equation, we expand the representation on vertically variable velocity media, which is the most common scenario in seismic exploration. The BCS based on this representation can be used to implement an irregular-grid increment finite-difference that improves the efficiency of RTM. Based on the Laplacian expression in Riemannian space, we derive the wave equation in the BCS. The new coordinate system can generate an irregular grid with increment increasing vertically along depth. Through paraxial ray tracing, it can be extended to non-analytical beam coordinate system (NBCS). Experiments for the RTM on the Marmousi model with the BCS demonstrate that the proposed method improves the efficiency about 52% while maintaining good image quality.

Keywords: beam coordinate system (BCS), reverse time migration (RTM), non-orthogonal coordinate system, Riemannian spaces

1. Introduction

Reverse time migration (RTM) is a popular method for creating accurate images in complex media and was initiated in the early 1980s (Baysal *et al.* 1983; McMechan 1983; Whitmore 1983). Numerical seismic modeling is the backbone of RTM since it can give an accurate representation of the wavefield in subsurface media for forward extrapolation of the source wavefield and back propagation of recorded wavefield. The finite-difference method is an important numerical seismic modeling tool for RTM (Baysal *et al.* 1983), and its mesh spacing affects the computation cost as well as the accuracy of the RTM method. Thus, increasing mesh spacing must be considered for improving the efficiency of RTM. There are several ways to achieve this. Most researchers (Holberg 1987; Igel *et al.* 1995; Yang *et al.* 2002; Etgen & O'Brien 2007; Liu 2013; Zhang & Yao 2013) introduce optimization differential operators to reduce the numerical dispersion and then use a large mesh spacing for finite differencing, but the uniform mesh spacing does not accord with the general velocity variation with depth in seismic

media. Some researchers (Moczo 1989; Jastram & Behle 1992; Jastram & Tessmer 1994; Wang *et al.* 2001; Chen & Xu 2012; Gao *et al.* 2018) have designed variable or irregular velocity model grids to reduce the overall sample points, which are more flexible for the real media and save much computation time for wave propagation modeling.

Irregular-grid finite differencing can be approached from different perspectives. Sava & Fomel (2004) proposed one-way wavefield extrapolation to semi-orthogonal distorted coordinate systems based on the theory in Riemannian spaces, which are general curvilinear coordinates. Shragge & Guojian (2008) thought Riemannian wavefield extrapolation could not be efficiently applied in pre-stack shot-profile migration algorithms because of coordinate systems continuously changing with sources and receivers. They proposed an analytical elliptical coordinate system. In seismic modeling, efficiency is among the priorities and the analytical irregular coordinate transformation is useful. Chen & Xu (2012) developed a numerical scheme based on a pyramid-shaped grid for elastic wave propagation for the pseudo-spectral implementation, the grid meshes are trapezoids in the 2D spaces, and the grid increment could change with depth. Their analytical irregular coordinate transformation can be related to Riemannian space, and the corresponding wave equations can be built easily. Gao *et al.* (2018) gave a detailed derivation of the second order acoustic wave equation in a trapezoid coordinate and solved the new equation with finite differences. Wu *et al.* (2018) derived the trapezoid coordinate acoustic wave equation with a CPML boundary condition. In this paper, we present a new non-orthogonal and analytical coordinate system, the beam coordinate system (BCS), which is similar to the pyramid-shaped or trapezoid coordinate system and can change grid increment with depth. Although the beam coordinate transformation is analytic, its implementation can be extended to a continuously changing velocity background like the ray coordinate system (Sava & Fomel 2004) because it is similar to Gaussian beam propagation and can be represented by paraxial rays.

This paper is organized as follows. First, with the introduction of the basic equation of optical Gaussian beam, the relationship between the new and the old coordinates is constructed according to the transformation equation. The extension of the coordinate transformation to a vertically variable velocity model is also achieved. Second, we build the wave equation in the BCS. Third, RTM is introduced into the BCS and the effectiveness of our equations for RTM is verified by the application of Marmousi synthetic data. Finally, the conclusions from this method and its implementation are put forward.

2. Beam coordinate system

2.1. The BCS

Gaussian beam optics is the study of the propagation of Gaussian beams through an optical system. For a Gaussian beam propagating in free space, the beam half width, w, defined as the distance away from the center axis of the beam, has a relationship with a distance z along the depth as

$$\frac{w^2}{w_0^2} - \frac{z^2}{z_R^2} = 1, \tag{1}$$

where the initial half width of beam w_0 is known as the beam waist, and the Rayleigh range z_R defined as the distance over which the beam width spreads by a factor of $\sqrt{2}$ is given by

$$z_R = \frac{\pi w_0^2}{\lambda}, \tag{2}$$

where λ is the wavelength; the beam width w will be replaced by the variable x in the following sections.

The beam profile in the 2D space (figure 1a) shows that the width of beam increases with the depth, and it meets the expectation of grid increment changes with the depth. Following the idea of the pyramid-shaped grid (Chen & Xu 2012), which is a trapezoid shape in the 2D space, we define a new non-orthogonal coordinate system(ξ_1, ξ_3), i.e. BCS, to denote (w_0, z) through equations (1) and (2). If the original coordinate is set to(x, z), the new coordinate ξ_1 is defined as a function of z and x:

$$\begin{cases} \xi_1 = \frac{x-a}{\sqrt{1+\gamma z_3^2}} \\ \xi_3 = z \end{cases}, \tag{3}$$

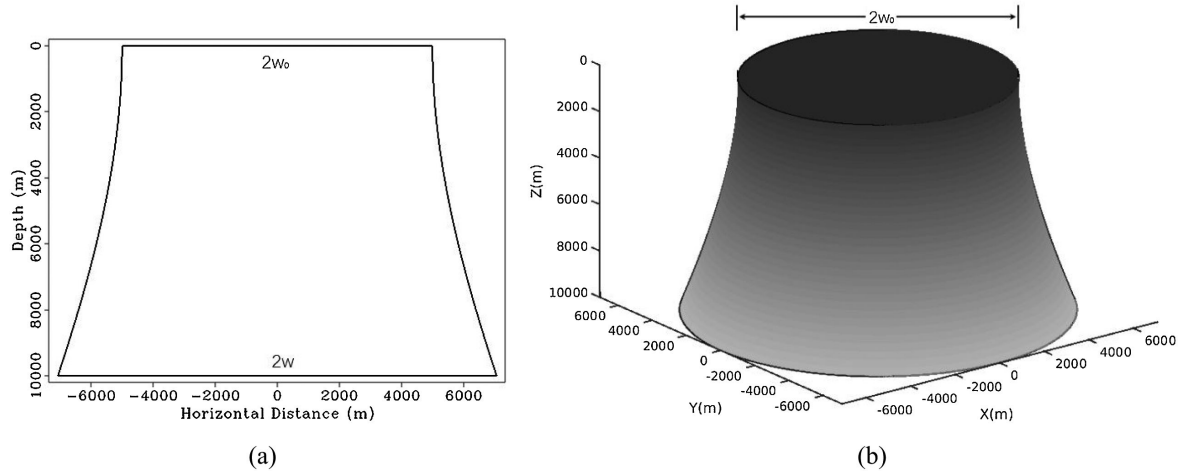

Figure 1. Optical Gaussian beam profiles: (a) 2D and (b) 3D. The initial beam half width w_0, called the beam waist of an optical Gaussian beam, increases with the depth direction along the z-axis, denoted by a variable w. The horizontal directions in the 3D coordinate system include the x- and y-axes.

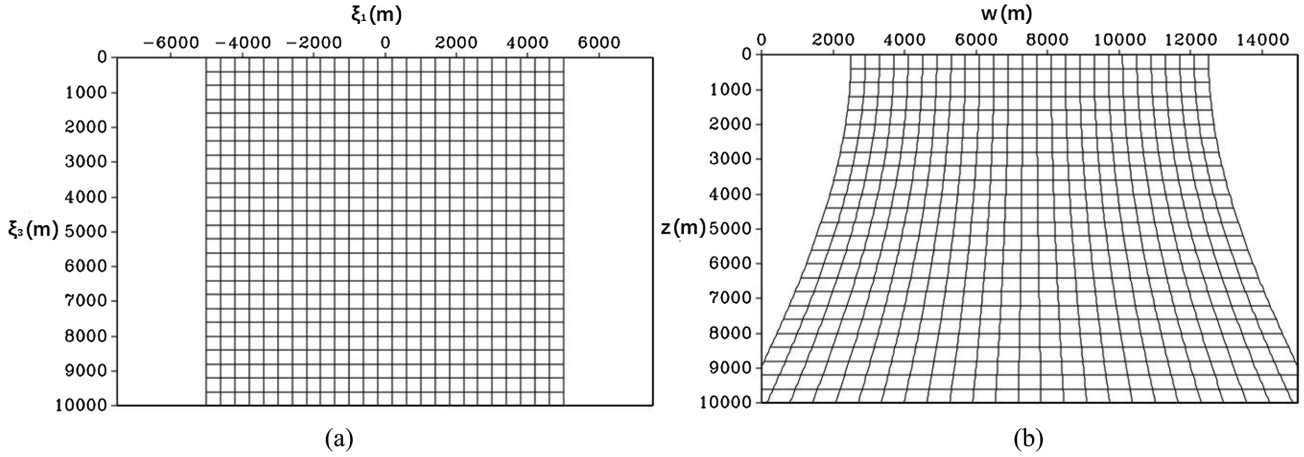

Figure 2. (a) The regular grid in the 2D BCS and (b) the corresponding irregular grid in the 2D CCS. The constant a is equal to 7500 m and $z_R = 8000$ m.

where the new coordinate ξ_1 is initiated from the beam width w_0, the constant a is a reference coordinate in the w-axis and the parameter γ is

$$\gamma = \frac{1}{z_R^2} = \frac{\lambda^2}{\pi^2 w_0^4}. \tag{4}$$

The regular grid (figure 2a) in the BCS of equation (3) has a mapping relationship with the irregular grid (figure 2b) in the Cartesian coordinate system (CCS). The variable γ is approximately equivalent to the square of the γ in the paper by Chen & Xu (2012).

The coordinate system (ξ_1, ξ_3) can be directly extended to the 3D spaces as the following equations:

$$\begin{cases} \xi_1 = \frac{x-a}{\sqrt{1+\gamma z_3^2}} \\ \xi_2 = \frac{y-b}{\sqrt{1+\gamma z_3^2}} \\ \xi_3 = z \end{cases}, \tag{5}$$

where the original Cartesian 3D coordinate system is defined as (x, y, z), the constants a and b are respective reference coordinates on the x- and y-axes. The corresponding Gaussian beam profile in the 3D space (x, y, z) is shown in figure 1b. Equation (5) is very similar to equation by Chen & Xu (2012) and can also be extended to the vertically variable velocity model

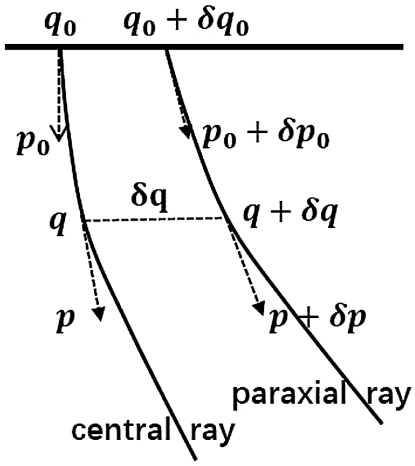

Figure 3. Central and paraxial rays in a ray-centered coordinate system $(\sigma,\ q)$ for a Gaussian beam. The variables $(\sigma,\ q)$ and p are the positions and slowness along the ray trajectory; δq and δp are perturbations of the position and slowness.

$c(z)$ as

$$\begin{cases} \xi_1 = \frac{x-a}{\sqrt{1+\gamma z_3^2}} \\ \xi_2 = \frac{y-b}{\sqrt{1+\gamma z_3^2}} \\ \xi_3 = \int_0^z \frac{c_0}{c(z)} dz \end{cases}. \tag{6}$$

Here, we set $c_0 = c(z = 0)$, which is the reference velocity model for generating the irregular coordinates. Similar to the ray coordinate system for an incident plane wave at the surface (Sava & Fomel 2004), our BCS is also not physical beam coordinates like those in the ray-centered coordinate system, and its coordinates $(\xi_1,\ \xi_2)$ are related to the initial width size of beam, $w_0^2 = \xi_1^2 + \xi_2^2$. Different from the ray coordinates, the coordinates $(\xi_1,\ \xi_2)$ are not orthogonal to the propagation ξ_3 axis, but the axes of ξ_1 and ξ_2 are mutually orthogonal. In this paper, we only examine the proposed method by using the 2D example, so it is a non-orthogonal coordinate system.

The new non-orthogonal coordinate systems (3), (5) and (6) are analytical and change uniformly from the original CCS to the new irregular coordinate system, so the source and receiver wavefields can share a common geometry, while non-analytical generalized curvilinear coordinate systems such as ray coordinate systems (Sava & Fomel 2004) have some problems, one of which is that the source and receiver wavefields do not share a common geometry (Shragge & Guojian 2008), which affects the computational efficiency. However, the forward and backward wavefields can propagate at angles relatively near the extrapolation in non-analytical generalized curvilinear coordinate systems and this improves the global accuracy of wavefield extrapolation (Shragge & Guojian 2008). Compared to the pyramid-shaped grids (Chen & Xu 2012) or trapezoid grids, our BCS can also be implemented in smoothed variable velocity by paraxial ray tracing (figure 3) and produces the non-analytical beam coordinate system (NBCS). The grid position and slowness of NBCS is written as

$$\begin{pmatrix} \delta q \\ \delta p \end{pmatrix} (\sigma) = \Pi(\sigma, \sigma_0) \begin{pmatrix} \delta q_0 \\ \delta p_0 \end{pmatrix}, \tag{7}$$

where the variables $(\sigma,\ q)$ and p are the positions and slowness along the ray trajectory in the ray-centered coordinate system; δq and δp are perturbations of the position and slowness; the matrix $\Pi(\sigma,\ \sigma_0)$ is the propagator matrix in dynamic ray tracing (Červený & Pšenčík 1983, 2010). So the NBCS $(\xi_1,\ \xi_3)$ is equal to $(q_0,\ \sigma)$ and q_0 should be a vector $(q_{10},\ q_{20})$ in the 3D space.

This NBCS is only one aspect of the extendibility of our irregular coordinate system, and also shows that the new coordinates have strict physical meaning for seismic wave propagation. The application of the NBCS will be further studied in the future. This paper focuses on the analytical BCS for RTM.

2.2. Wave equation in the beam coordinate system

In 3D Riemannian spaces, the Laplacian operator of the acoustic wave equation (Sava & Fomel 2004) has the form

$$\nabla^2 u = \sum_{i=1}^{3} \frac{1}{\sqrt{|\boldsymbol{g}|}} \frac{\partial}{\partial \xi_i} \left(\sum_{j=1}^{3} g^{ij} \sqrt{|\boldsymbol{g}|} \frac{\partial u}{\partial \xi_j} \right), \tag{8}$$

where u is the wavefield of the acoustic wave equation, ξ_i are the beam coordinates, g^{ij} are elements of the inverse of metric tensor, i.e.

$$\left[g^{ij}\right] = \left[g_{ij}\right]^{-1}, \tag{9}$$

and $|\boldsymbol{g}| = |det(g_{ij})|$ is absolute value of its determinant. The elements of the metric tensor are defined as

$$g_{ij} = \frac{\partial x_k}{\partial \xi_i} \frac{\partial x_k}{\partial \xi_j} = \left[J^T J\right]_{ij}, \tag{10}$$

where x_k are the Cartesian coordinates. Equation (10) is the metric tensor for the coordinate x_k. J is the Jacobian matrix for $\xi_i \rightarrow x_i$.

From equation (6), the Jacobian matrix of equation (10) can be attained as

$$\left[J^{ij}\right] = \begin{bmatrix} \sqrt{1+\gamma z^2} & 0 & \frac{c(\xi_3)}{c_0} \frac{\gamma \xi_1 z}{\sqrt{1+\gamma z^2}} \\ 0 & \sqrt{1+\gamma z^2} & \frac{c(\xi_3)}{c_0} \frac{\gamma \xi_2 z}{\sqrt{1+\gamma z^2}} \\ 0 & 0 & \frac{c(\xi_3)}{c_0} \end{bmatrix}, \tag{11}$$

where the depth z in the original coordinate system is a function $z(\xi_3)$ of ξ_3, which can be inverted from $\xi_3 = \int_0^z \frac{c_0}{c(z)} dz$ and model $c(z)$. Inserting equation (11) into (10) and inverting the metric tensor $\left[g_{ij}\right]$, to give its determinant

$$|\boldsymbol{g}| = \frac{c^2(\xi_3)}{c_0^2} \left(1+\gamma z^2\right)^2 \tag{12}$$

and its inverse

$$\left[g^{ij}\right] = \begin{bmatrix} \frac{\left(1+\gamma z^2\right)+\gamma^2 z^2 \xi_1^2}{\left(1+\gamma z^2\right)^2} & \frac{z^2 \gamma^2 \xi_1 \xi_2}{\left(1+\gamma z^2\right)^2} & -\frac{c_0}{c(\xi_3)} \frac{\gamma \xi_1 z}{1+\gamma z^2} \\ \frac{z^2 \gamma^2 \xi_1 \xi_2}{\left(1+\gamma z^2\right)^2} & \frac{\left(1+\gamma z^2\right)+\gamma^2 z^2 \xi_2^2}{\left(1+\gamma z^2\right)^2} & -\frac{c_0}{c(\xi_3)} \frac{\gamma \xi_2 z}{1+\gamma z^2} \\ -\frac{c_0}{c(\xi_3)} \frac{\gamma \xi_1 z}{1+\gamma z^2} & -\frac{c_0}{c(\xi_3)} \frac{\gamma \xi_2 z}{1+\gamma z^2} & \frac{c_0^2}{c^2(\xi_3)} \end{bmatrix}. \tag{13}$$

According to equations (8), (12) and (13), the 3D wave equation in the BCS is written as follows,

$$\begin{aligned} \frac{1}{v^2} \frac{\partial^2 u}{\partial t^2} = & \frac{3\gamma^2 z^2 \xi_1 - \frac{c_0}{c(\xi_3)} \gamma \xi_1 \left(1+\gamma z^2\right)}{\left(1+\gamma z^2\right)^2} \frac{\partial u}{\partial \xi_1} + \frac{\left(1+\gamma z^2\right)+\gamma^2 z^2 \xi_1^2}{\left(1+\gamma z^2\right)^2} \frac{\partial^2 u}{\partial \xi_1^2} + \frac{3z^2 \gamma^2 \xi_2 - \frac{c_0}{c(\xi_3)} \gamma \xi_2 \left(1+\gamma z^2\right)}{\left(1+\gamma z^2\right)^2} \frac{\partial u}{\partial \xi_2} \\ & + \frac{2z^2 \gamma^2 \xi_1 \xi_2}{\left(1+\gamma z^2\right)^2} \frac{\partial^2 u}{\partial \xi_1 \partial \xi_2} - \frac{c_0}{c(\xi_3)} \frac{2\gamma \xi_1 z}{\left(1+\gamma z^2\right)} \frac{\partial^2 u}{\partial \xi_1 \partial \xi_3} + \frac{\left(1+\gamma z^2\right)+\gamma^2 z^2 \xi_2^2}{\left(1+\gamma z^2\right)^2} \frac{\partial^2 u}{\partial \xi_2^2} - \frac{c_0}{c(\xi_3)} \frac{2\gamma \xi_2 z}{\left(1+\gamma z^2\right)} \frac{\partial^2 u}{\partial \xi_2 \partial \xi_3} \\ & - \frac{c_0^2}{c^2(\xi_3)} \frac{\partial c(\xi_3)}{\partial \xi_3} \frac{\partial u}{\partial \xi_3} + \frac{c_0^2}{c^2(\xi_3)} \frac{\partial^2 u}{\partial \xi_3^2}. \end{aligned} \tag{14}$$

Simplifying equation (14) to 2D spaces, gives

$$\frac{1}{v^2}\frac{\partial^2 u}{\partial t^2} = \frac{3\gamma^2 z^2 \xi_1 - \frac{c_0}{c(\xi_3)}\gamma\xi_1\left(1+\gamma z^2\right)}{\left(1+\gamma z^2\right)^2}\frac{\partial u}{\partial \xi_1} + \frac{\left(1+\gamma z^2\right)+\gamma^2 z^2 \xi_1^2}{\left(1+\gamma z^2\right)^2}\frac{\partial^2 u}{\partial \xi_1^2} - \frac{c_0}{c\left(\xi_3\right)}\frac{2\gamma\xi_1 z}{\left(1+\gamma z^2\right)}\frac{\partial^2 u}{\partial\xi_1\partial\xi_3} + \frac{c_0^2}{c^2\left(\xi_3\right)}\left[\frac{\partial^2 u}{\partial \xi_3^2} - \frac{\partial c\left(\xi_3\right)}{\partial \xi_3}\frac{\partial u}{\partial \xi_3}\right]. \tag{15}$$

Equation (15) includes the reference velocity model $c(z)$ or $c(\xi_3)$ that generates the coordinates in the BCS for the wave equation. We need to switch this model between the CCS and BCS through interpolation method while implementing the program for wave propagation, which produces some errors in the depth position and the spatial derivative of velocity. The new coordinate systems do not need to be created with the same velocity model as the one used for migration (Sava & Fomel 2004). So it makes the above equations simpler to use with a constant gradient reference velocity model:

$$c\left(z\right) = c_0 + \beta z, \tag{16}$$

where the constant β is velocity gradient. Equation (16) is put into equation (6) to give

$$\xi_3 = ln\left(1+\frac{\beta z}{c_0}\right). \tag{17}$$

Further, we obtain the function

$$z = \frac{c_0}{\beta}\left(e^{\xi_3}-1\right). \tag{18}$$

Thus,

$$\frac{\partial c\left(\xi_3\right)}{\partial \xi_3} = c_0\, e^{\xi_3}. \tag{19}$$

The constant gradient reference velocity model for generating the irregular coordinates satisfies the desired objective that makes the finite-difference grid increment increase with depth.

2.3. *Reverse time migration*

Compared with one-way wave equation migration, RTM uses the exact two-way wave equation, including all seismic wavefield types, and theoretically can offer by far the most accurate imaging results for complex media among all the seismic migration methods. RTM requires the several key steps: the forward extrapolation of the source wavefield, back propagation of the recorded wavefield and imaging by using an imaging condition. Here a standard explicit finite-difference method is implemented for wavefield forward or backward propagation in the BCS. In equation (13) or (14), the finite-difference approximation for the first and second space partial derivative of wavefield can be written as

$$\begin{cases} \dfrac{\partial u}{\partial \xi_1} = \dfrac{\sum_{p=1}^{N} c_p\left(u_{i+p,j,k}^t - u_{i-p,j,k}^t\right)}{\Delta\xi_1} \\ \dfrac{\partial^2 u}{\partial \xi_1^2} = \dfrac{\sum_{p=1}^{N} d_p\left(u_{i+p,j,k}^t + u_{i-p,j,k}^t - 2u_{i,j,k}^t\right)}{\left(\Delta\xi_1\right)^2} \end{cases}, \tag{20}$$

where i, j, k are, respectively, the grid indices along the ξ_1, ξ_2, ξ_3 axes. The variable c_p and d_p are, respectively, the optimized finite-difference coefficients for the first and second derivatives. The time derivative of wavefield is replaced with a second order finite difference and the mixed derivative such as $\frac{\partial^2 u}{\partial\xi_1\partial\xi_3}$ can be changed to a combination of second order partial derivatives (Guan *et al.* 2011).

After reconstructing the forward wavefield $S(t;\ \xi_1,\ \xi_2,\ \xi_3)$ from the source and back propagation wavefield $G(t;\ \xi_1,\ \xi_2,\ \xi_3)$ extrapolated from the recorded data, the RTM image is constructed by using the cross-correlation imaging condition,

$$I\left(\xi_1,\xi_2,\xi_3\right) = \int_0^T S\left(t;\ \xi_1,\xi_2,\xi_3\right) G\left(t;\ \xi_1,\xi_2,\xi_3\right) dt, \tag{21}$$

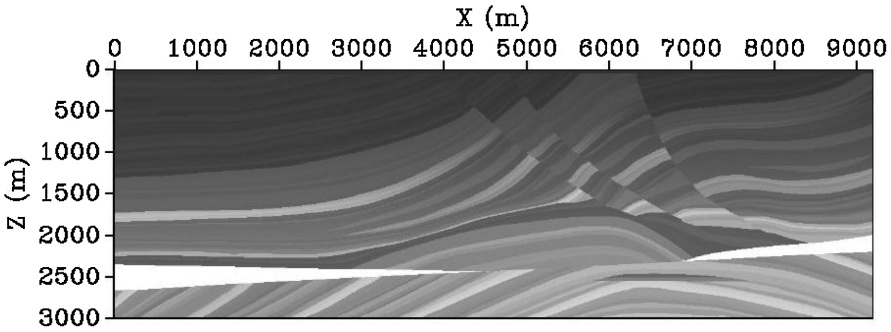

Figure 4. The Marmousi model: the grid mesh is 461 × 751, the intervals are, respectively, 20 m and 4 m in the *x* and z coordinates.

where $I(\xi_1, \xi_2, \xi_3)$ is the image at the position (ξ_1, ξ_2, ξ_3) and T is the maximum time of propagation of the wavefield. Through a sinc interpolation step, the final image in the CCS can be obtained from the image $I(\xi_1, \xi_2, \xi_3)$.

3. Numerical example

To demonstrate RTM in the BCS, a linear $v(z)$ model and the Marmousi synthetic data are used to test our method. The $v(z)$ model with $v(z) = (1500 + 1550 \times z/3.0)$ m s^{-1} has the same dimensions and grid parameters with the following Marmousi model and is used to verify the accuracy of forward modeling through the wavefield snapshots. The Marmousi model and geometry were created to produce complicated seismic data that require advanced processing techniques to obtain a correct earth image (Irons 2014). Figure 4 shows the Marmousi velocity model for the grid mesh 461 × 751 with the intervals 20 m and 4 m in the *x* and *z* coordinates, which will be interpolated to the finer interval in the *x*-axis for modeling. The data contain 751 sample points in time at a time sampling of 4 ms, 176 shots along the *x*-axis position 3000–7200 m with a source sampling of 24 m, and 261 receivers per shot along the *x*-axis 2000–7200 m with receiver sampling of 20 m. Next, we run the BCS RTM on this model and data to test the viability of the proposed coordinate system for improving the efficiency.

The BCS is global for the whole model, so the wavelength λ should have a large scale and is not dependent on the data frequency or the model velocity. We only need to keep the increase of the grid spacing of the BCS with depth. According to equation (5) or (6), the parameter γ can be obtained from:

$$\frac{\Delta x\,(z_{max})}{\Delta x\,(z_{min})} = \frac{\sqrt{1+\gamma z_{max}^2}}{\sqrt{1+\gamma z_{min}^2}} = \mu \frac{v_{min}\,(z_{max})}{v_{min}\,(z_{min})}, \tag{22}$$

where μ is a constant. Equation (22) indicates that the ratio of the beam coordinate grid spacing between the maximum depth z_{max} and the minimum depth z_{min} in the CCS is proportional to the minimum velocity v_{min} ratio between the minimum and the maximum depth. So,

$$\gamma = \frac{\left[\beta \frac{v_{min}(z_{max})}{v_{min}(z_{min})}\right]^2 - 1}{z_{max}^2 - \left[\beta \frac{v_{min}(z_{max})}{v_{min}(z_{min})}\right]^2 z_{min}^2} = \frac{\left[\beta \frac{v_{min}(z_{max})}{v_{min}(z_{min})}\right]^2 - 1}{z_{max}^2}. \tag{23}$$

Using equations (4) and (23), the Rayleigh range can be expressed as

$$z_R = \frac{1}{\sqrt{\left[\beta \frac{v_{min}(z_{max})}{v_{min(z_{min})}}\right]^2 - 1}} z_{max}. \tag{24}$$

The constant velocity gradient for the new coordinate system is also constructed by using the minimum velocity v_{min} as

$$\beta = \frac{v_{min}\,(z_{max}) - v_{min}\,(z_{min})}{z_{max} - z_{min}}. \tag{25}$$

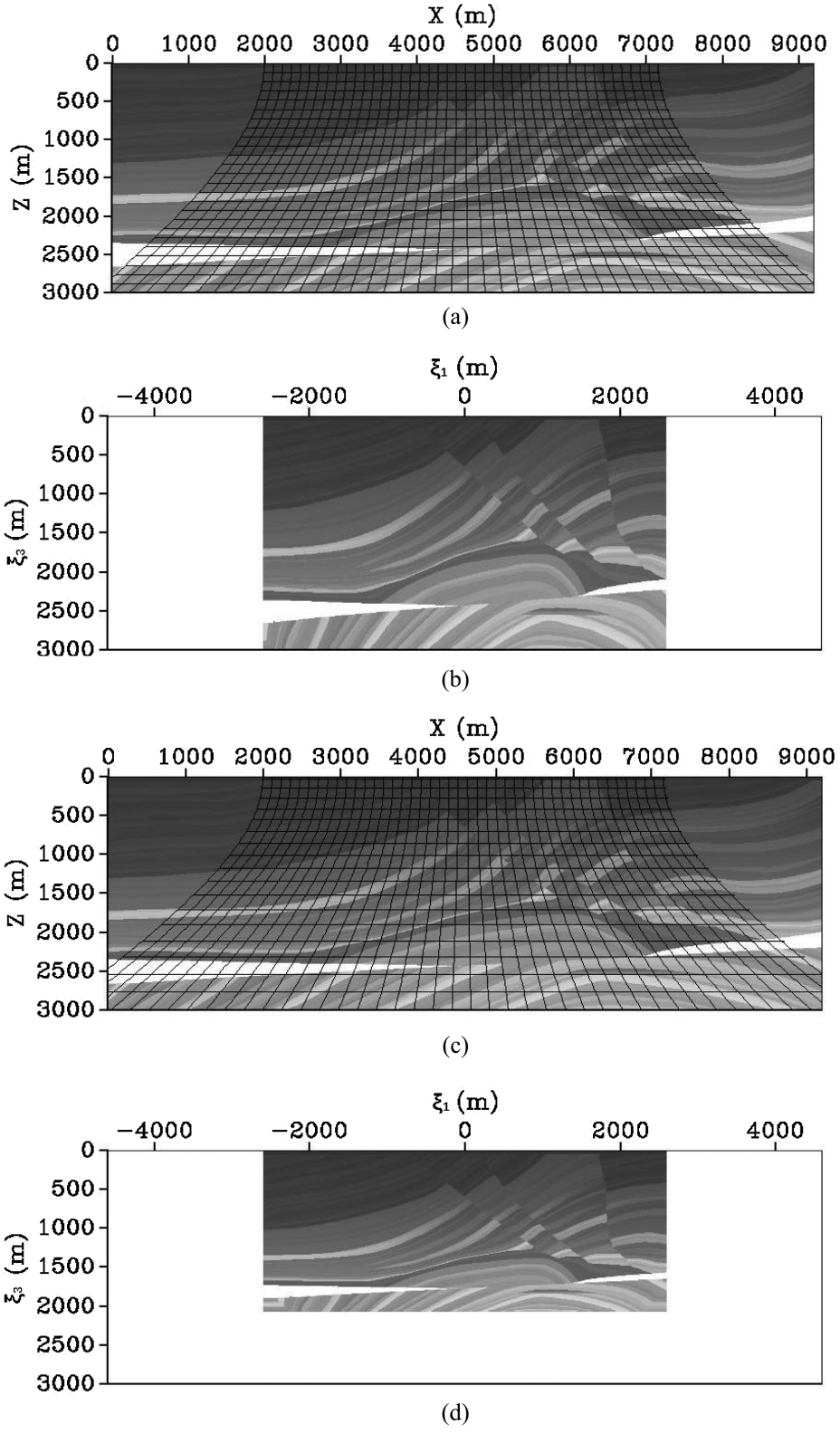

Figure 5. The Marmousi model: (a) the beam grids overlay the model in the CCS for case 3; (b) the model in the BCS for case 3; (c) the beam grids overlay the model in the CCS for case 4 and (d) the model in the BCS for the case 4.

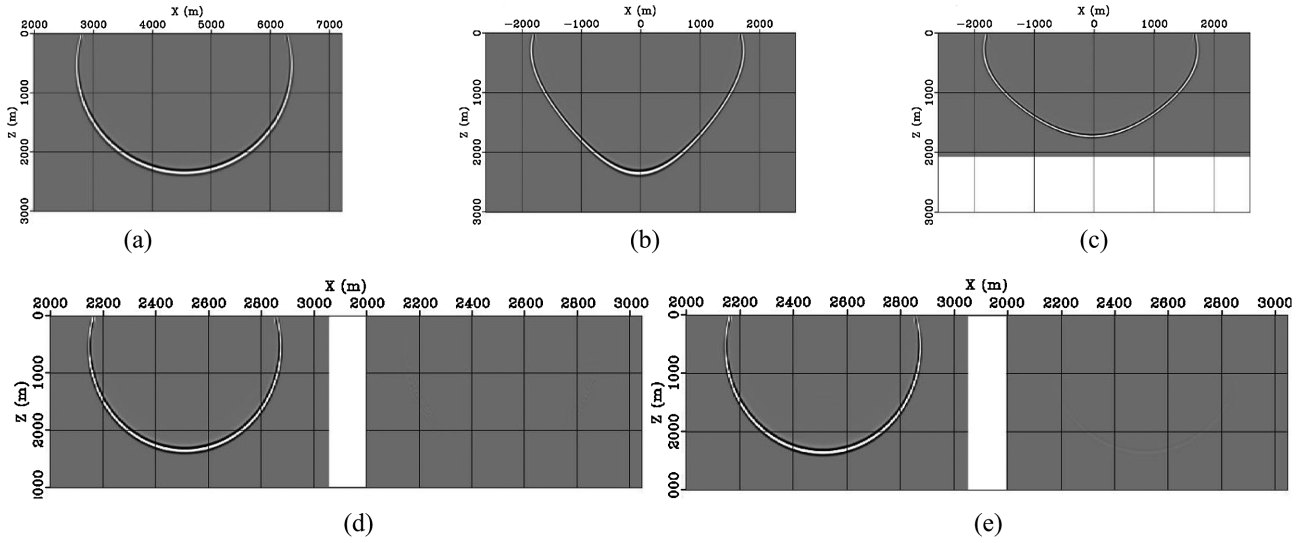

Figure 6. Wavefield snapshot comparisons the time 1.24 s in the $v(z)$ model. (a) The wavefield snapshot in the CCS. (b) Case 1: the wavefield snapshot in the BCS. (c) Case 2: the wavefield snapshot in the BCS. (d) the left is the wavefield snapshot interpolating (b) into the CCS and the right is the difference in results between the left and (a). (e) The left is the wavefield snapshot interpolating (c) into the CCS and the right is the difference of results between the left and (a).

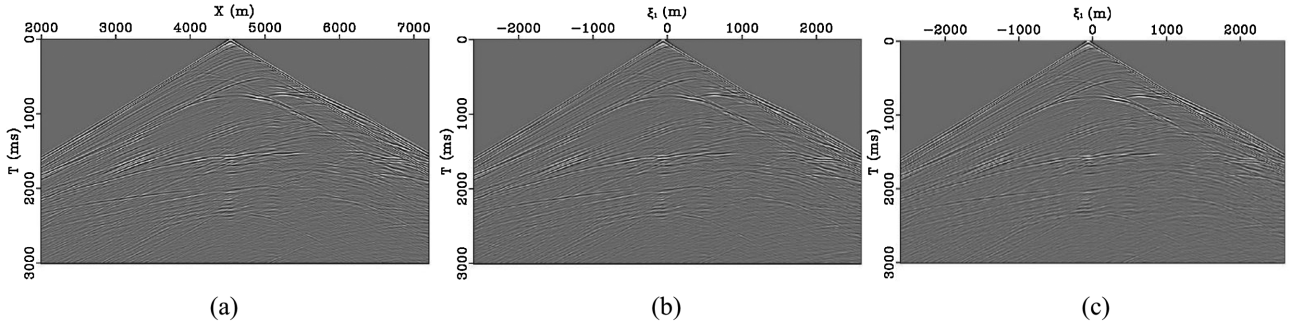

Figure 7. Synthetic data comparison of shot no. 65 in the Marmousi model: (a) the data in the CCS; (b) the synthetic data of forward-propagation of RTM in the BCS for case 3 and (c) the synthetic data of forward-propagation of RTM in the BCS for case 4. The beam coordinates initiate from the same surface positions with the Cartesian, so they should have the same record.

Thus,

$$\begin{cases} c_0 = v_{min}\,(z_{min}) \\ c\,(z) = c_0 + \beta z \end{cases}. \tag{26}$$

The tests on the $v(z)$ model have the same parameters in equation (26) with the Marmousi model for the coordinate system transformation in equation (5) or (6). Here, set $a = 4600$ m, ξ_1 from -2600 to 2600 m and test four cases:

Case 1: the $v(z)$ model with $c = c_0$ and $\mu = 0.9$;
Case 2: the $v(z)$ model with $c = c(z)$ in equation (26) and $\mu = 1.0$.
Case 3: the Marmousi model with $c = c_0$ and $\mu = 0.9$;
Case 4: the Marmousi model with $c = c(z)$ in equation (26) and $\mu = 1.0$.

The constant μ is not an important point for the four tests. We get the beam coordinate grids (figure 5a) in the CCS for case 1 or case 3, the Marmousi model in the BCS for case 3 (figure 5b), the beam coordinate grids (figure 5c) in the CCS for case 2 or case 4, and the Marmousi model in the BCS with 517 points in depth for case 4 (figure 5d). The beam coordinate grids shown in figure 5a and c overlap the Marmousi model. The $v(z)$ models in the BCS for case 1 and case 2 have a similar layout to the Marmousi model shown in figure 5b and d.

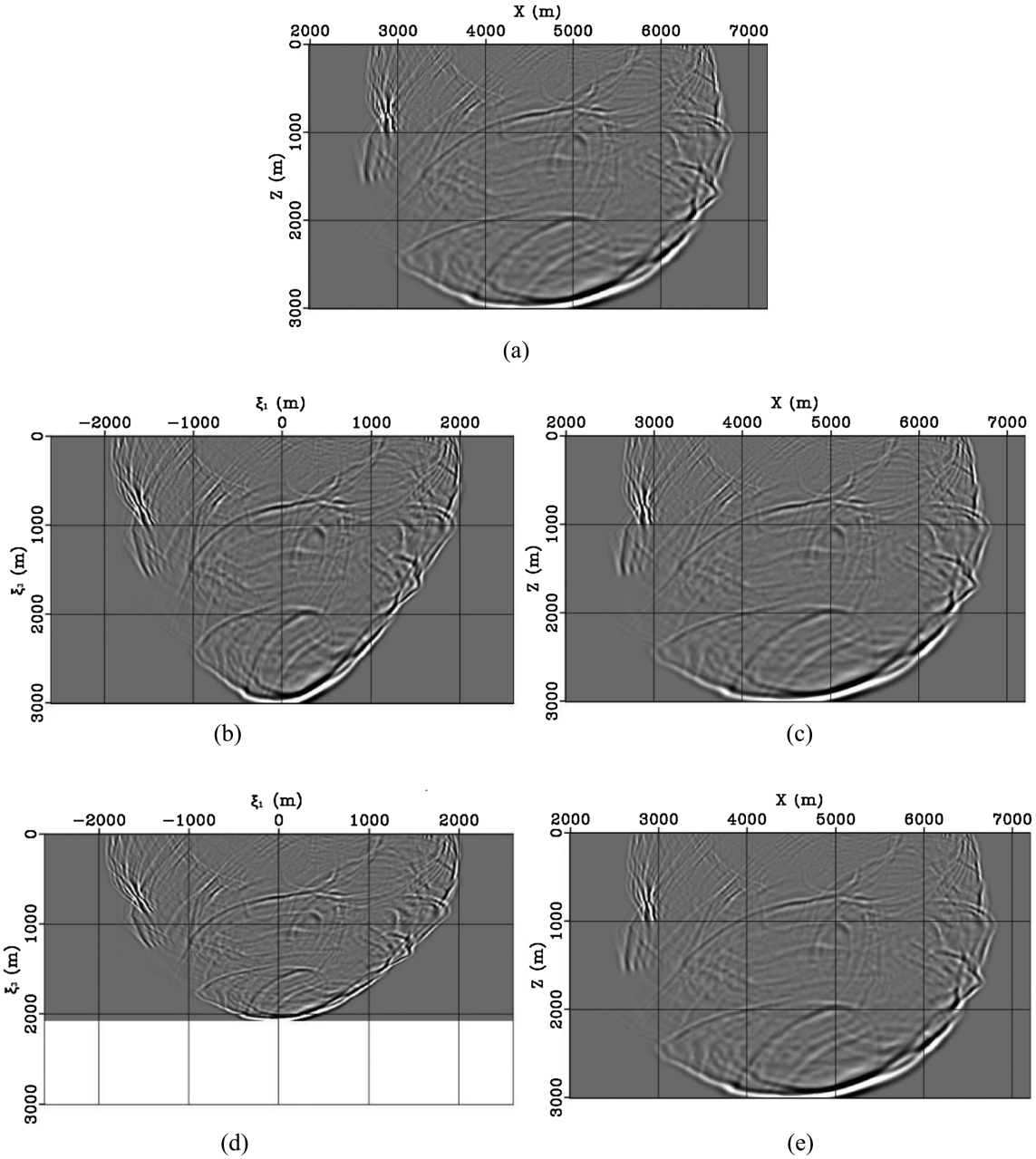

Figure 8. Wavefield snapshot comparisons of shot no. 65 shot at the time 1.24 s in the Marmousi model. (a) The wavefield snapshot in the CCS; (b) Case 3: the wavefield snapshot of forward-propagation for RTM in the BCS; (c) Case 3: the wavefield snapshot interpolating (b) into the CCS; (d) Case 4: the wavefield snapshot of forward-propagation for RTM in the BCS and (e) Case 4: the wavefield snapshot interpolating (d) into the CCS.

In the BCS, the forward extrapolation of the source wavefield and back propagation of the recorded wavefield are executed through the finite-difference algorithm of the wave equation (15), and the final seismic image is constructed by correlating the source and data wavefields and subsequently using post-processing, such as low-pass filtering. Before testing the wave propagation and imaging in the Marmousi model, the comparison between wavefield snapshots of the $v(z)$ velocity model in the CCS (figure 6a) and in the BCS for case 1 (figure 6b) or for case 2 (figure 6c) is to show the reliability of the new coordinate systems. The snapshot for case 1 (the left of figure 6d) interpolating from figure 6b and its difference (the right of figure 6d) from figure 6a shows the same display parameters, and the difference can obviously be ignored. So, the BCS for case 1 only introduces small errors relative to the CCS. For case 2, the left of figure 6e is the snapshot interpolating from figure 6c and the right of figure 6e is the difference between the left and figure 6a. The amplitude of difference in figure 6e is a little stronger than the right of figure 6d and vertical transformation especially introduces more interpolation errors, but it is still very weak.

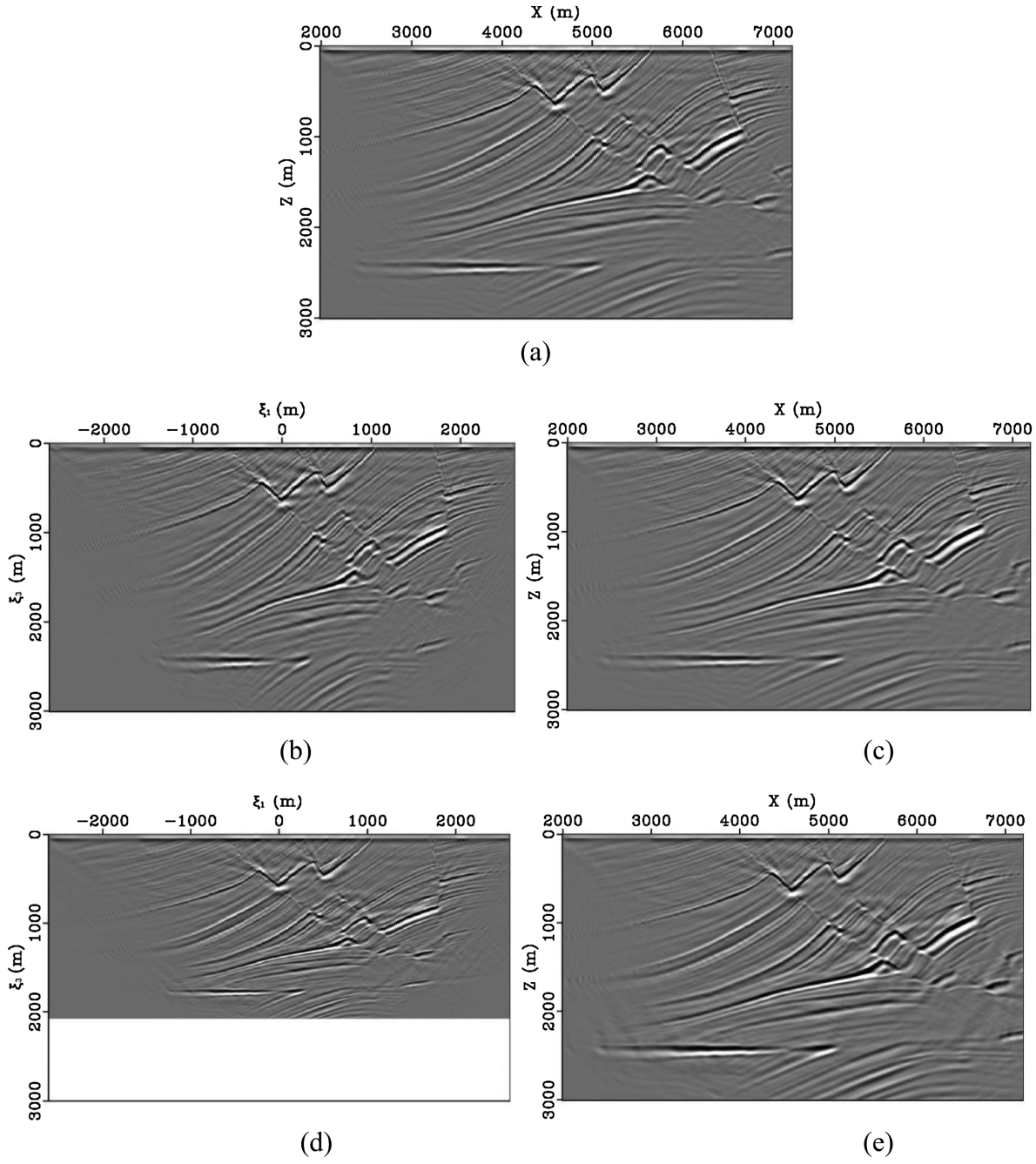

Figure 9. The Marmousi imaging results: (a) RTM in the CCS; (b) Case 3: RTM in the BCS; (c) Case 3: the result interpolating the result of (b) into the CCS; (d) Case 4: RTM in the BCS and (e) Case 4: the result interpolating the result of (d) into the CCS.

To further validate the implementation of finite-difference forward modeling in the BCS, the record and wavefield snapshots of the Marmousi are compared with each other in two coordinate systems. Figure 7 shows the shot no. 65 data record in the CCS and the synthetic data of forward-propagation for RTM in the BCS. The beam coordinates initiate from the same surface positions as the CCS, so they should model the same data. Compared with the data in figure 7a, the synthetic record in figure 7b only has more dispersion noise and does not handle the artificial bounding condition reflections well, which are reasonable because of larger grid spacing. The wavefield snapshot for case 3 (figure 8b) in the BCS appears more narrow than the one (figure 8a) in the CCS. The result for case 3 (figure 8b) interpolating from the former is almost the same as the one (figure 8a) in the CCS. For the test in case 4, the wavefield snapshot (figure 8d) in the BCS is short in the depth because it only has 517 sample points compared with 751 sample points in the CCS. The result (figure 8e) interpolating from the figure 8d is almost the same as the one (figure 8a) in the CCS.

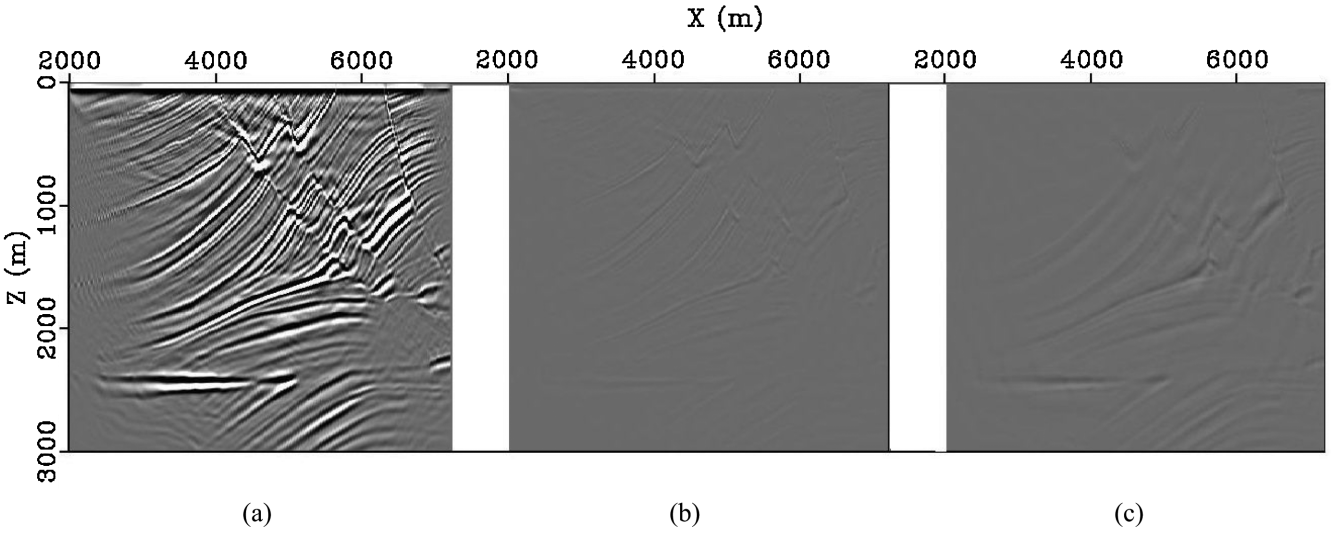

Figure 10. (a) The Marmousi imaging result of RTM in the CCS, which is same as figure 9a; (b) the difference in results between figure 9c and figure 9a and (c) the difference in results between figure 9e and a.

To check the RTM method in the BCS, it is very useful to make a comparison in quality and efficiency between the RTM results in the CCS and those in the BCS. The final Marmousi imaging result (figure 9c) interpolating from the RTM result (figure 9b) in the BCS for case 3 is comparable to that in the CCS in the quality, and only has differences on the fault facet (figure 10b). For case 3, this meets expectations in terms of efficiency, and the algorithm based on the new coordinate system saves about 35% of time consumption because of reducing grid number by 43.5% while increasing the computation load in the finite-difference items. We can also reduce the computation time through limiting the image range along the lateral direction in the CCS, which is equivalent to decreasing the lateral grid number. For case 4, it reduces the grid number not only in the lateral direction but also in the vertical direction. So it should bring more improvement in the efficiency of RTM, and one shot migration only needs 52% computation time in the CCS. The final image (figure 9e) interpolating from the result in the BCS (figure 9d) for the case 4 has comparable quality in the same way. From figure 9e and figure 10c, the amplitude of the RTM result for case 4 in the depth is stronger than those of figure 9a and c. It shows that the BCS for case 4 might bring better illumination for imaging.

4. Discussion

The BCS is similar to the pyramid-shaped grids in 3D spaces (Chen & Xu 2012) and the trapezoid-shaped grids in the 2D space (Gao *et al.* 2018). So far, the BCS only provides an alternative to the irregular-grid forward modeling for seismic imaging. In fact, as mentioned in the introduction, the NBCS can be implemented through the paraxial ray tracing like the ray coordinate system (Sava & Fomel 2004), which is an advantage of the BCS for further application. A further application might be one-way wavefield extrapolation like the ray coordinate system (Sava & Fomel 2004), or Gaussian beam forward modeling and imaging implementation and so on.

5. Conclusion

A new irregular coordinate system named BCS is introduced because its coordinates are related to the optical Gaussian beam equation, which can also be extended to a heterogeneous background velocity through paraxial ray tracing. A successful implementation of RTM in the BCS is achieved. First, based on the Laplacian expression in the Riemannian spaces, wave equations can be directly expressed in the BCS. Second, the conventional RTM steps includes forward extrapolation of the source wavefield; back propagation of the recorded wavefield and imaging are implemented in the BCS. Third, the final image is attained by interpolating the above results to the CCS.

According to the numerical experiments for the synthetic data of the Marmousi model, we prove that RTM in the BCS can reduce computation time through reasonably increasing the grid spacing with depth in finite differencing. The results for cases 3 and 4 in this paper can, respectively, save about 35 and 52% of time for one shot forward modeling. The snapshot

comparison of cases 1 and 2 in the $v(z)$ model shows the BCS introduces some errors but they are still with reasonable range. The forward modeling of the Marmousi models in the BCS can be implemented by a finite-difference numerical method, but obvious boundary reflections appear in the synthetic data or the wavefield snapshot, therefore a better absorbing boundary algorithm, such as perfectly matched layer (Wu *et al.* 2018), should be combined in the above process. The BCS aims at modeling on variable and large mesh spacing dependent on the variable velocity to reduce the computation time. When applying in complex media, this might involve more numerical errors and result in loss of accuracy.

Acknowledgements

This work was supported by the Center for Postdoctoral Studies at China University of Petroleum (East China), the sponsorship of the National Natural Science Foundation of China (41774137), the Qingdao Postdoctoral Applied Research Project (05T1801003) and the National Oil and Gas Major Projects of China (2017ZX 05032003). For the results in this paper, we used some tools, such as filtering, interpolating and plotting, and the Marmousi model in the Madagascar open-source platform (www.ahay.org), and are grateful to all its developers.

Conflict of interest statement. None declared.

References

Baysal, E., Kosloff, D.D. & Sherwood, J.W.C., 1983. Reverse time migration, *Geophysics*, **48**, 1514–1524.

Červený, V. & Pšenčík, I., 1983. Gaussian beams and paraxial ray approximation in three-dimensional elastic inhomogeneous media, *Journal of Geophysics*, **53**, 1–15.

Červený, V. & Pšenčík, I., 2010. Gaussian beams in inhomogeneous anisotropic layered structures, *Geophysical Journal International*, **180**, 798–812.

Chen, F. & Xu, S., 2012. Pyramid-shaped grid for elastic wave propagation, in *the 82nd Annual International Meeting of the Society of Exploration Geophysicists, Expanded Abstracts, 2012*, SEG, USA, p. 890.

Etgen, J.T. & O'Brien, M.J., 2007. Computational methods for large-scale 3D acoustic finite-difference modeling: a tutorial, *Geophysics*, **72**, SM223–SM230.

Gao, J., Xu, W., Wu, B., Li, B. & Zhao, H., 2018. Trapezoid grid finite difference seismic wavefield simulation with uniform depth sampling interval. *Chinese Journal of Geophysics. (in Chinese)*, **61**, 3285–3296.

Guan, H., Dussaud, E., Denel, B. & Williamson, P., 2011. Techniques for an efficient implementation of RTM in TTI media, in *the 81st Annual International Meeting of the Society of Exploration Geophysicists, Expanded Abstracts*, p. 3393.

Holberg, O., 1987. Computational aspects of the choice of operator and sampling interval for numerical differentiation in large-scale simulation of wave phenomena, *Geophysical Prospecting*, **35**, 629–655.

Igel, H., Mora, P. & Riollet, B., 1995. Anisotropic wave propagation through finite-difference grids, *Geophysics*, **60**, 1203–1216.

Irons, T., 2014. Marmousi Model. Madagascar Datasets, Reproducible Documents, Madagascar wiki. Available at: http://www.reproducibility.org/RSF/book/data/marmousi/paper_html/, last accessed 17 August 2018.

Jastram, C. & Behle, A., 1992. Acoustic modeling on a grid of vertically varying spacing, *Geophysical Prospecting*, **40**, 157–169.

Jastram, C. & Tessmer, E., 1994. Elastic modelling on a grid with vertically varying spacing, *Geophysical Prospecting*, **42**, 357–370.

Liu, Y., 2013. Globally optimal finite-difference schemes based on least squares, *Geophysics*, **78**, T113–T132.

McMechan, G.A., 1983. Migration by extrapolation of time-dependent boundary values, *Geophysical Prospecting*, **31**, 413–420.

Moczo, P., 1989. Finite-difference technique for SH-waves in 2-D media using irregular grids-application to the seismic response problem. *Geophysical Journal International*, **99**, 321–329.

Sava, P. & Fomel, S., 2004. Wavefield extrapolation in Riemannian coordinates, in *the 74th Annual International Meeting of the Society of Exploration Geophysicists, Expanded Abstracts*, p. 1049.

Shragge, J. & Guojian, S., 2008. Prestack wave-equation depth migration in elliptical coordinates, *Geophysics*, **73**, S169–S175.

Wang, Y., Xu, J. & Schuster, G.T., 2001. Viscoelastic wave simulation in basins by a variable-grid finite-difference method, *Bulletin of the Seismological Society of America*, **91**, 1741–1749.

Whitmore, N.D., 1983. Iterative depth migration by backward time propagation, in *the 53th Annual International Meeting of the Society of Exploration Geophysicists, Expanded Abstracts*, p. 382.

Wu, B., Xu, W., Jia, J., Li, B., Yang, H., Zhao, H. & Gao, J., 2018. Convolutional perfect matched layer boundary for trapezoid grid finite difference seismic modeling, in *the 88th Annual International Meeting of the Society of Exploration Geophysicists, Expanded Abstracts*, p. 3989.

Yang, D.H., Liu, E., Zhang, Z.J. & Teng, J., 2002. Finite-difference modelling in two-dimensional anisotropic media using a flux-corrected transport technique. *Geophysical Journal International*, **148**, 320–328.

Zhang, J.H. & Yao, Z.X., 2013. Optimized explicit finite-difference schemes for spatial derivatives using maximum norm, *Journal of Computational Physics*, **250**, 511–526.